ADVANCED ENGINEERING MATERIALS
www.aem-journal.com

Examination of the Oxidation and Metal–Oxide Layer Interface of a Cr–Nb–Ta–V–W High Entropy Alloy at Elevated Temperatures

*Rebecca Romero, Nanthakishore Makeswaran, Ravisankar Naraparaju, and Chintalapalle V. Ramana**

The authors report on the evaluation of the oxide scale and the interface microstructure of a Cr–Nb–Ta–V–W refractory high entropy alloy (HEA) at elevated temperatures. The Cr–Nb–Ta–V–W HEA is oxidized at 700 and 800 °C in lab air and the substrate/oxide interface is investigated. Combined in situ X-ray diffraction (XRD) coupled with ex situ scanning electron microscopy (SEM) and energy dispersive X-ray spectrometry (EDS) analyses characterize the oxide scale and confirm the phases present in the substrate which have been previously identified in this alloy. The microstructure near the interface is studied for an indication of selective oxidation of this alloy. Cracking and porosity are found along the interface layer which grows directionally outward. Two main oxides are identified: a W-based oxide with a needle-like structure and a Cr oxide containing Ta that has a granular structure, primarily found in clusters. The oxide layers are porous, and no dense protective oxide is identified. It is found that when the temperature is increased to 800 °C, the oxide layer exhibits an increase in thickness. In situ XRD indicates that V is the first element to oxidize.

1. Introduction

As new technologies emerge and operating temperatures increase, the limits of what current materials can withstand are pushed and the demand for alloys with exceptional properties grows. Alloy design specifically for high-temperature applications continues to be an emerging field in materials design and manufacturing, specifically in the power generation and nuclear industries. A growth in such industries has made it essential that material components be able to operate and bear excellent properties at such elevated temperatures. The concept of high entropy alloys (HEAs) proposed by Yeh et al. is useful for the design of new alloys capable of operating at elevated temperatures.[1–4] The objective was to create a new approach to alloy design, focusing on systems with multiple principal elements in equimolar or near-equimolar ratios rather than one principal element. The alloy system may be simply defined as one containing at least five elements in equiatomic proportion, though there are various definitions that may exist. HEAs may also be defined by an entropy-based definition based on the magnitude of the total configurational entropy.[5] The main concept is aimed at promoting the formation of a single-phase-disordered solid solution that is stabilized by configurational entropy.[6] Much of the HEA research has focused on producing a single-phase solid solution, though HEAs have the potential to contain two or more phases and may contain a mixture with an intermetallic phase. Various reviews of HEAs can be found in the literature.[5,7–9]

Research has indicated that HEAs can have excellent strength.[10] For example, a higher yield strength value was obtained from the HfMoNbTaTiZr HEA compared with two nickel-based superalloys at elevated temperatures. HEA research has also indicated that they can have a high corrosion resistance and fracture strength and obtain thermal stability since being proposed.[11,12] For instance, for $AlCoCrFeNiTi_x$ alloys (x: molar ratio; $x = 0$, 0.5, 1, 1.5) the microstructures of which were body-centered cubic (BCC) solid solutions at all given Ti compositions except $Ti_{1.5}$ which is BCC–Laves, the alloys displayed excellent strength at room temperature.[13] The compressive yield stress values are in the range from 1.5 to 2.26 GPa at room temperature, of which the $AlCoCrFeNiTi_{0.5}$ obtained the highest value while also obtaining a fracture strength of 3.14 GPa and exhibiting excellent plastic strain of 23.3%. The obtained mechanical properties made them superior to the comparable high strength bulk alloys reported and were attributed to the solid

R. Romero, Dr. N. Makeswaran, Prof. C. V. Ramana
Center for Advanced Materials Research
University of Texas at El Paso
500 West Univ. Avenue, El Paso, TX 79968, USA
E-mail: rvchintalapalle@utep.edu

R. Romero
Department of Metallurgical, Materials and Biomedical Engineering
University of Texas
500 West Univ. Avenue, El Paso, TX 79968, USA

Dr. N. Makeswaran, Dr. R. Naraparaju
German Aerospace Center (DLR)
Institute of Materials Research
Cologne 51 170, Germany

Prof. C. V. Ramana
Department of Mechanical Engineering
University of Texas
500 West Univ. Avenue, El Paso, TX 79968, USA

The ORCID identification number(s) for the author(s) of this article can be found under https://doi.org/10.1002/adem.202100164.

DOI: 10.1002/adem.202100164

solution strengthening mechanism of the Ti atom. The promise of impressive mechanical properties of HEAs in comparison with conventional alloys at room temperature prompted further research of processing and properties of this class of alloys at elevated temperatures.

The search for the retention of strength and stability at elevated temperatures of HEAs gave rise to the concept of refractory HEAs (RHEAs) originally proposed by Senkov et al.[14] The objective of RHEAs research is to create a class of materials primarily based on refractory element constituents such as Mo, Ta, W, Nb, and V.[14] The main reason for using refractory elements is due to their high melting temperatures, which would increase the overall melting temperature of the alloy and thus increase the maximum operating temperature. The objective of creating RHEAs would be to replace commonly used superalloys, which are limited by their solvus and melting temperatures up to 1000 °C.[14] Within the past decade, several studies have been conducted to further investigate many of these RHEAs. For example, Senkov et al. first reported the mechanical properties and microstructures of different refractory HEAs at elevated temperatures.[15,16] They found that both the $Nb_{25}Mo_{25}Ta_{25}W_{25}$ and $V_{20}Nb_{20}Mo_{20}Ta_{20}W_{20}$ alloys exhibit the ability to retain strength at temperatures up to 1600 °C. When compared with two commonly used superalloys, both novel alloys were able to achieve a higher yield stress above 800 °C, reaching ≈550 and 850 MPa at 800 °C. The decrease in yield stress as temperature increased was also considered to be rather weak. In the temperature range from 600 to 1600 °C, a decrease from 561 to 405 MPa for the $Nb_{25}Mo_{25}Ta_{25}W_{25}$ alloy and from 862 to 470 MPa for the $V_{20}Nb_{20}Mo_{20}Ta_{20}W_{20}$ was seen. The encouraging results of the first RHEAs stimulated future studies. The mechanical properties of a $V_{35}Ti_{35}Fe_{15}Cr_{10}Zr_5$ alloy were investigated and found to have excellent ductility at elevated temperatures.[17] At temperatures of 800 and 900 °C, the alloy did not fracture after a compression strain of >12% was applied. This was significantly greater than seen at room temperature. The alloy also exhibited yield strengths ≈500 MPa higher than comparable alloys used for fusion applications (ODS Steel, F82H, V–4Cr–4Ti, and CLAM). It reached a peak value of 1238 MPa at 500 °C. Since then, various studies have been conducted to evaluate the mechanical properties of RHEAs at elevated temperatures.[18–20]

Though several HEAs have proven to be useful at high temperatures because of their high strength and microstructural stability at elevated temperatures, the environmental behavior characteristics must also be considered.[15–18,21] Despite having high melting points, refractory metals have poor oxidation resistance at high temperatures, which has limited their ability to be implemented in commercial applications. The strategy used by RHEAs has awarded the opportunity to enhance the oxidation resistance through high concentrations of alloying elements.[14] Elements known for benefiting oxidation resistance (Al, Cr, Si, and Ti) may also be added for further resistance. Gorr et al. studied the oxidation behavior of a 20Mo–20 W–20Al–20Cr–20Ti alloy displayed, despite containing 40% refractory metals.[22] After exposure to laboratory air for 40 h at 1000 °C, the alloy followed a parabolic rate law of the mass change. It was determined that the evaporation of Mo and W negligibly small or inhibited by the oxide layer that formed, indicating that the alloy did not suffer from catastrophic oxidation. Hardness values indicated the potential ductile nature of the alloy at room temperature, as no cracks were seen in either the dendritic or interdendritic regions. After annealing for 40 h at 1200 °C, the hardness increased from ≈685 HV in dendritic regions and ≈330 HV in interdendritic regions, to ≈800 HV and exhibited a more homogeneous microstructure. The oxidation behavior of different compositions of equiatomic alloys was also studied by the Gorr et al., which also exhibited relatively good oxidation resistance.[23,24] When compared with commercial refractory alloys (a linear mass gain of ≈100 mg cm^{-2} h^{-1}) at temperatures up to 1100 °C, all the alloys studied had a lower specific mass gain of <10 mg cm^{-2} (after 48 h oxidation in air). Though many of the oxidation studies performed have focused on RHEAs because of their poor elemental oxidation resistance, however, there has been expansion to include study the oxidation of nonrefractory containing HEAs. Al–Co–Cr–Ni–Fe and Al–Co–Cr–Ni–Si HEAs were investigated for the oxidation behavior up to 1050 °C.[25] It was found that the oxidation behavior was dictated by the amounts of Al and Cr, which was related to the growth of the protective Al_2O_3 and Cr_2O_3 scales. The results found were comparable with observations made for similar Ni-based superalloys.[26]

The static and cyclic oxidation of the Cr–Nb–Ta–V–W alloy along with the microstructural stability has been previously studied, but the oxidation behavior has not yet been fully characterized.[21,24] To further understand the chemical composition and oxide morphology, the substrate–oxide layer interface and oxide surface were studied. The HEA was subjected to in situ X-ray diffraction (XRD) at temperatures up to 800 °C to determine the early-stage oxidation behavior of individual elements, including potential protective oxide formation. A cross-sectional examination of the oxide/metal interface was conducted to show any indications of selective oxidation and evaluate the microstructure of the oxide layer. The surface layer of the oxide was also analyzed using energy dispersive X-ray spectrometry (EDS) and XRD, as well as a physical oxide analysis to evaluate the shape and sizes of the oxides present. Thus, a combined in situ structural and ex situ microstructure and chemical analysis allowed the authors to examine and confirm the oxide phases and the alloy–oxide interface microstructure.

2. Results and Discussion

2.1. Cross-Sectional Substrate–Oxide Interface—SEM

The alloy composition was confirmed to be near-nominal, consisting of a 20.7% W–20.4% V–20.0% Cr–19.7% Nb–19.3% Ta alloy.[21] While more details of the as-received samples can be found in the study by Varma et al.,[21] the information on the microstructure of the HEA is briefly outlined below for the purpose of clarity and to understand the oxidation induced microstructure variations. The as-received HEA samples exhibit a multiphase microstructure, where at least five areas correspond to their morphological and compositional differences identified. The large globules contain a W-rich phase with, perhaps, Cr and V in solid solutions. Cloudy or shaded phases but with a variable darkness. The light cloudy areas were Nb-rich, while the dark areas were V-rich. Based on EDS analyses, it was concluded that the cloudy microconstituents are mixtures of two phases, either Nb- or V-rich. Another distinctly different area was identified as a

Cr-rich solid solution of Cr–Ta in a more or less grainy morphological form (gray area) containing an intermetallic compound.

The microstructure of the substrate–oxide layer interface of the oxidized sample at 700 °C for 24 h can be seen in **Figure 1**. EDS spot analysis was performed to estimate the composition of different areas. The bulk microstructure of the as-received condition in the study by Varma et al.[21] was considered as the basis of this study, as the material was the same. Medium gray areas, marked as B and C in Figure 1, are visible within the substrate near the interface previously identified as phase 3. The areas of phase 3 consist of a Cr-rich structure containing a mixture of a Ta–Cr solid solution and a Laves phase.[21] This is confirmed by EDS in the area marked B. Within these areas labeled B and C, there is some cracking and porosity visible within the phase 3. A darker grey area is visible just to the left of area B within the substrate, marked A. This area A is suspected to be a Ta-rich oxide as shown by the EDS analysis performed. Figure 1 includes the elemental analysis, indicating the presence of this potentially Ta-rich oxide. The oxide layer itself exhibits some uniformity with evidence of porosity and cracking throughout the layer near the interface. An area labeled D within the oxide layer near the interface contains all of the constituent elements, and a significant amount of oxygen about 64%. There is W, Ta, and V all present within the area of D. The large, dark pore near the bottom left-hand corner of the image is similar in shape and morphology of a VO_x pore which was identified in an $NbCrMoTiVAl_{0.5}$ alloy.[27] The VO_x pores identified in the $NbCrMoTiVAl_{0.5}$ alloy were found to have most likely formed because of fusion or volatilization of a V_2O_5 oxide. A low melting point of V_2O_5 at 670 °C is likely to have been a contributing factor to this.[28] The author's suspect that the large pore identified near the interface in Figure 1 may be of similar formation.

Figure 2 confirms the presence of the three phases (1, 3, and 4) previously identified within the substrate.[21] Phase 1 is a W-rich phase containing trace amounts Cr, V, and Ta. Phase 4 is a cloudy Nb-rich phase in solid solution with V, Cr, and Ta and phase 3 is a Cr phase in solid solution with Ta. The areas believed to be these phases are noted in Figure 2 as X and Y—Nb- and W-enriched areas are found around the Cr-rich areas. Both Ta and Cr elements appear to stay in solution in the substrate and do have a strong presence in the oxide layer, which is evident in the EDS elemental mapping. Cracking and voids are present at the interface boundary which grow upward into the oxide layer and are indicated in Figure 2. Nb and W are the two main elements which appear the most in the oxide layer. There is no significant constituent element within the oxide layer. A Nb-rich mixed oxide was found just above the interface at location A, while a W-rich oxide was found in the center of the oxide layer as the area marked B where Cr, V, and Ta were present in similar amounts in both the oxides. Location C and D are representative of the previously identified phase 3 which is a (Cr,Ta)-rich phase. Location E is believed to be like the previously identified phase 1, which is a W-rich phase, though W is not as prominent as previously found. Location F is previously identified phase 4 which is a cloudy, Nb-rich phase with a solid solution of V, Cr, and Ta and small amounts of W. Indications of a V-rich phase are seen in the substrate near the interface. Voids at the boundary layer that grow into the oxide layer are indicated in the figure.

Figure 3 shows the nonuniformity of the oxide layer, which appears as a thick, porous layer. The pores are suspected to be linked to the presence of W and Ta in the oxide layer in areas near each other because of the difference in coefficient of thermal expansion (CTE).[29,30] When there is a large difference in CTE, one oxide may cool faster, which in this case is W, and causes a difference in contraction leaving a void space. In this case, W has a CTE of approximately 4.8×10^{-6}, while Ta has a CTE of approximately 6.7×10^{-6}. Tungsten appears vertically in the oxide layer, indicating an upward directional growth of the oxide layer. This is visible through the EDS elemental mapping where strings of W appear throughout the layer. Ta clusters around neighboring regions of W in the oxide layer.

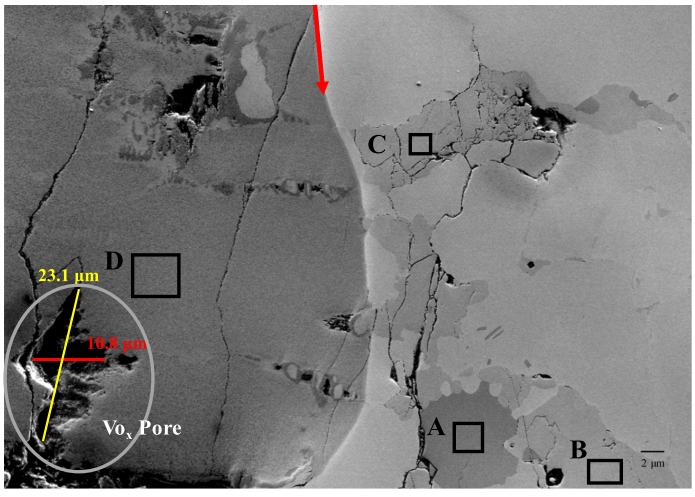

	A	B	C	D
O	62.13	3.08	5.99	63.73
V	11.71	11.00	12.42	7.66
Cr	0.71	45.14	42.27	4.21
Nb	0.89	9.27	5.04	3.38
Ta	23.46	24.39	26.44	10.10
W	1.11	7.13	7.83	10.92
Total	100.0	100.0	100.0	100.0

Figure 1. Microstructure of a cross section of the substrate–oxide interface of the oxidized sample at 700 °C for 24 h in secondary electron (SE) mode. The boundary line between the substrate and oxide layer is indicated by the red arrow, the substrate is to the right (light gray), and the oxide layer is to the left (dark grey). Cracking and porosity are visible just below and within the oxide interface. Local EDS analysis was also performed in four areas noted in the figure. The atomic percentage of each element is outlined in the corresponding table.

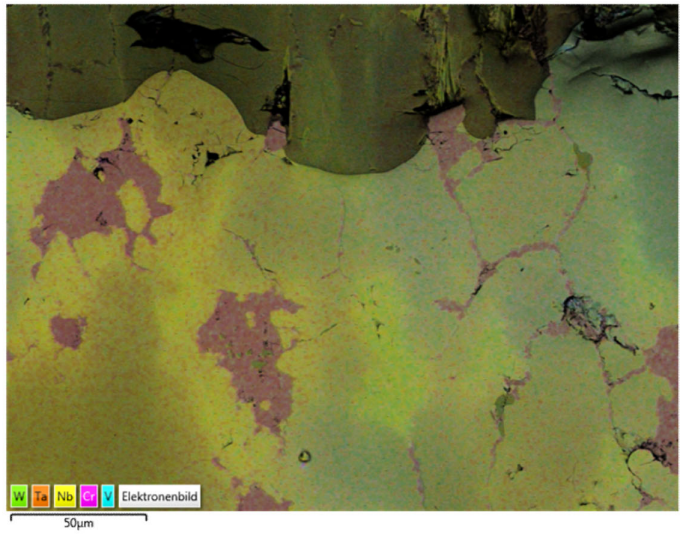

	A	B	C	D	E	F
O	64.36	66.28	0.0	0.0	6.08	11.04
V	5.70	5.34	10.93	12.12	10.31	9.85
Cr	6.38	4.24	47.33	46.17	11.06	12.86
Nb	11.20	6.08	9.78	7.05	13.47	51.96
Ta	6.94	5.61	23.36	26.84	24.79	11.08
W	5.42	12.44	8.59	7.82	34.29	3.21
Total	100.0	100.0	100.0	100.0	100.0	100.0

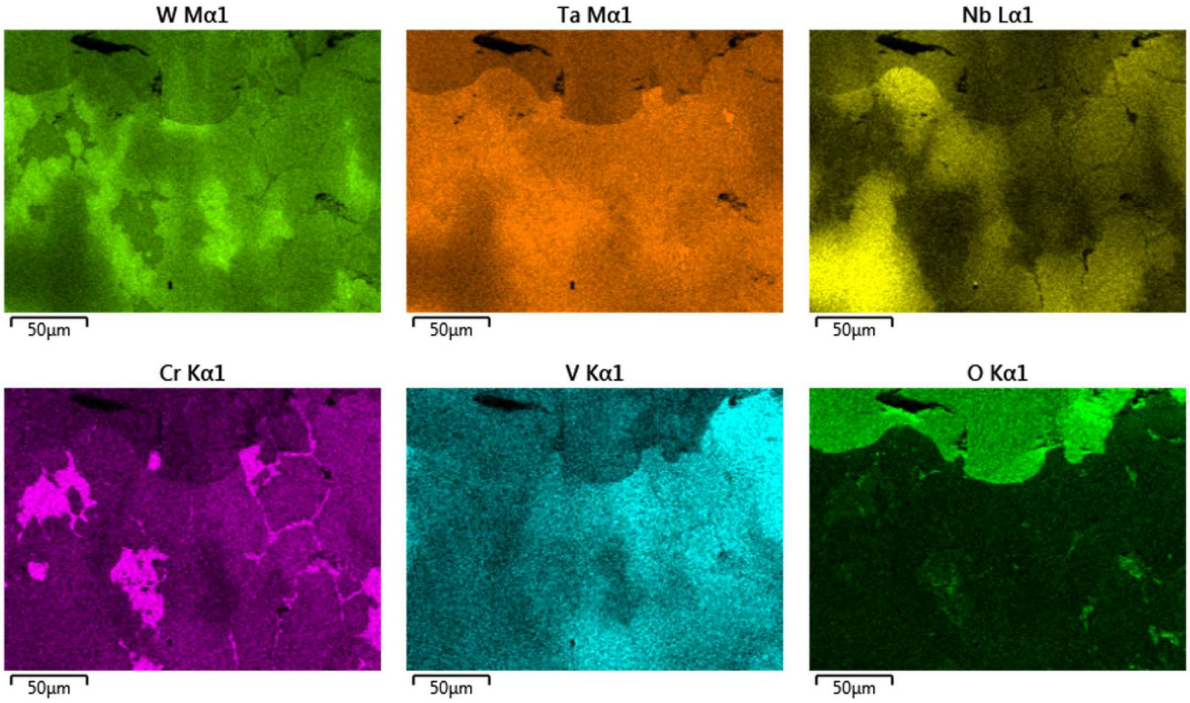

Figure 2. Substrate–oxide interface of the oxidized sample at 700 °C for 24 h in backscatter electron (BSE) mode with EDS elemental mapping and point analysis. Various areas throughout the substrate and within the oxide layer are marked and the atomic percentage of each area is noted in the corresponding table.

Clusters of a W–Ta oxide appear above the surface layer and within some of the large pores, which is highlighted in the mapping. Nb, Cr, and V appear to remain in solution in the substrate, except for Cr, which appears in small amounts throughout the oxide layer. **Figure 4** shows the thickness of the grown oxide layer, which shows large variation along the surface. The thickness ranges from 391.2 to 461.1 µm and is found to be little less than those measured of the alloy CrMoNbTaV, which ranged from 530 to 1132 µm, though these measurements were taken at temperatures in the range of 900–1100 °C for 25 h.[31]

The cross section of the interface of the oxidized sample at 800 °C for 24 h is shown in **Figure 5**. A significant amount of porosity and separation crack appears at the interface, like what was seen at 700 °C, possibly due to the occurrence of spallation. The porosity is once again believed to be a result of a V-oxide which melted or the difference in CTE between Ta and W. No single element appears to predominate in the oxide layer, though there are areas of a Cr-rich and W-rich oxide dispersed throughout. **Figure 6** shows a similar oxide layer to that at 700 °C, which is nonuniform and porous in nature. V appears in small clusters, closer to the interface area and center of the oxide layer.

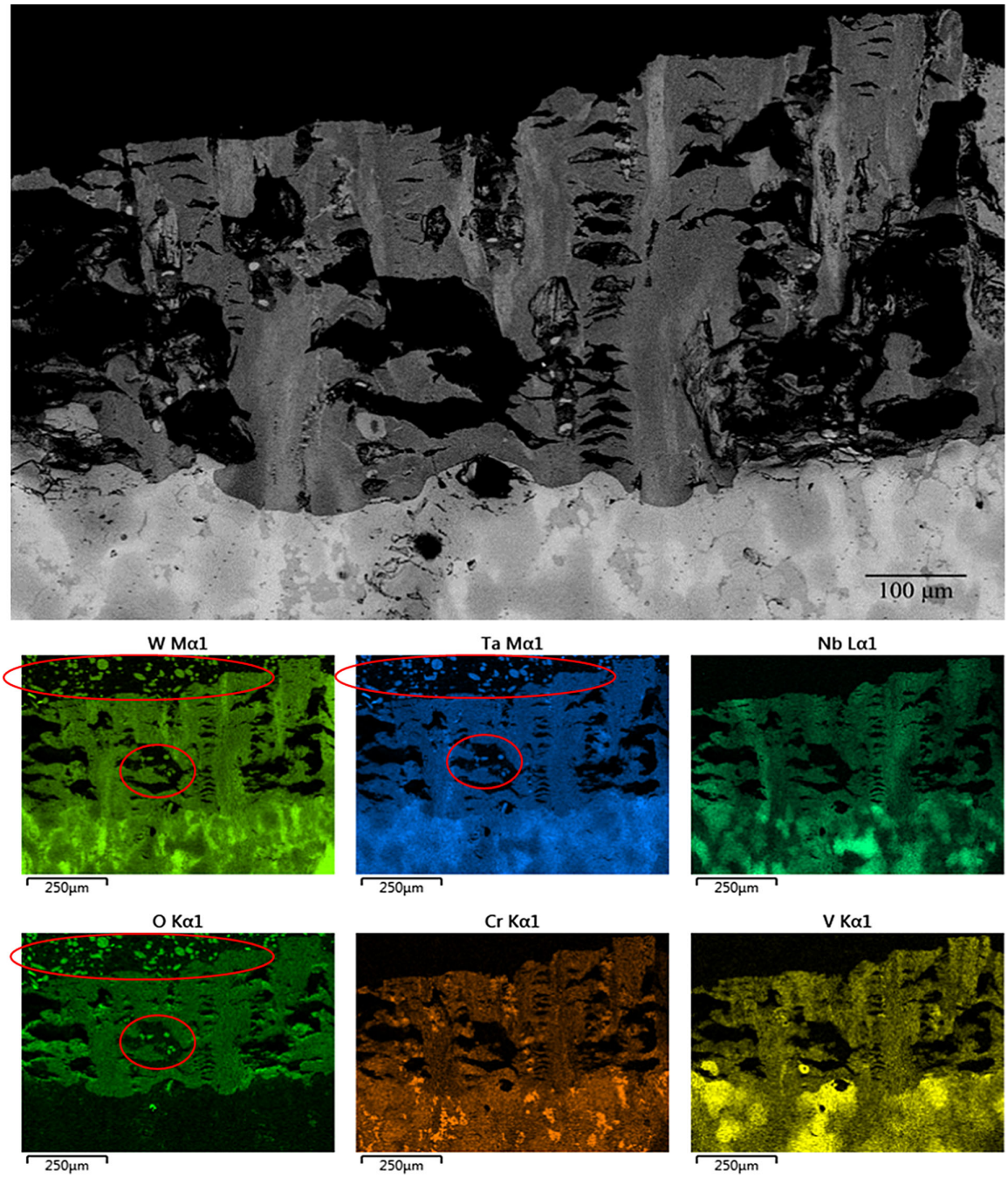

Figure 3. Substrate–oxide interface of the oxidized sample at 700 °C after 48 h in the BSE mode with corresponding EDS elemental mapping. Significant amounts of porosity are visible within the oxide layer. Lighter W oxides are present in the oxide layer as the lighter vertical areas in the layer with small clusters of Ta in neighboring regions. An area of W–Ta clusters appears above the surface of the oxide layer and in regions between the voids.

There is no V that appears at the surface of the oxide layer. W again shows a linear, directional upward growth from the interface dispersed throughout the oxide layer. Cr appears in clusters spread relatively evenly throughout the oxide layer. Nb and Ta do not appear heavily throughout the oxide layer; however, Ta remains in the substrate just below the interface. **Figure 7** shows the thickness of the oxide layer, which is relatively even. The thickness was measured in the range from 1.313 to 1.379 mm.

2.2. Surface Analysis—SEM

Additional surface analysis of the oxide layers was performed to examine the morphology and chemical composition of oxide scales grown at 700 and 800 °C after 48 h to compare with the cross-sectional analysis. At both temperatures, the oxides show a similar physical morphology; however, the oxide layer is denser, containing less porous space, on the 800 °C sample.

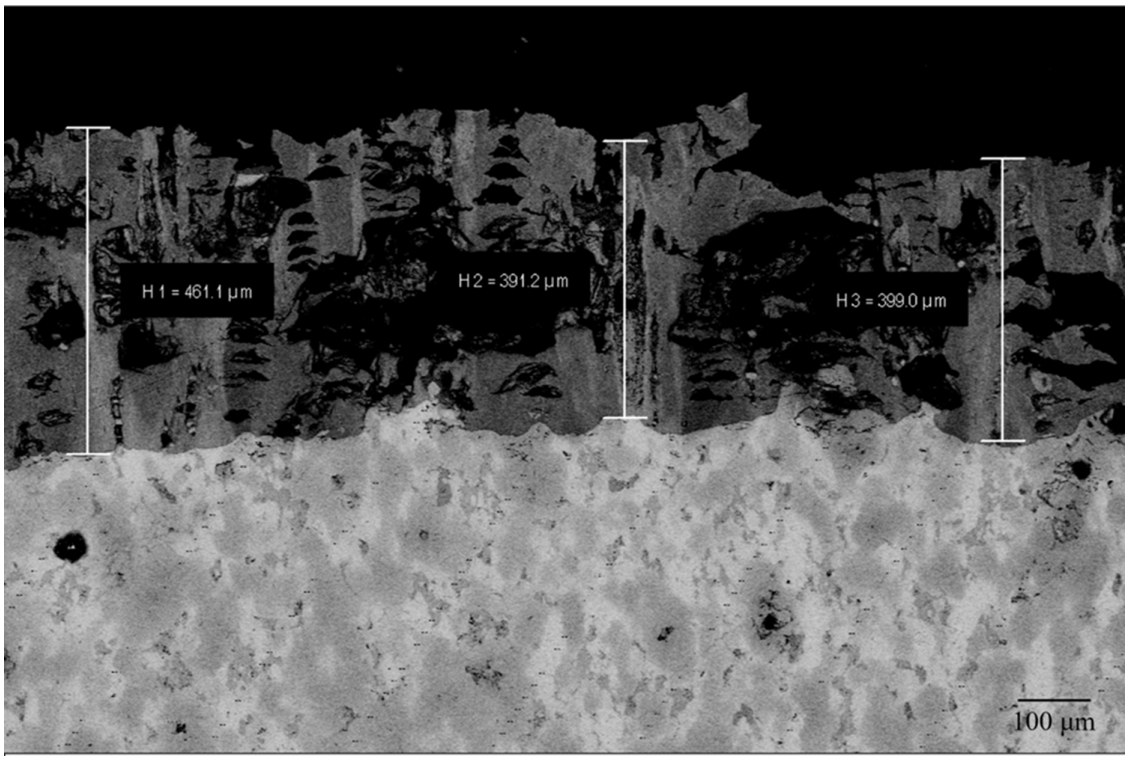

Figure 4. Substrate-oxide interface of the oxidized sample at 700 °C in the BSE mode indicating the thickness of the oxide layer.

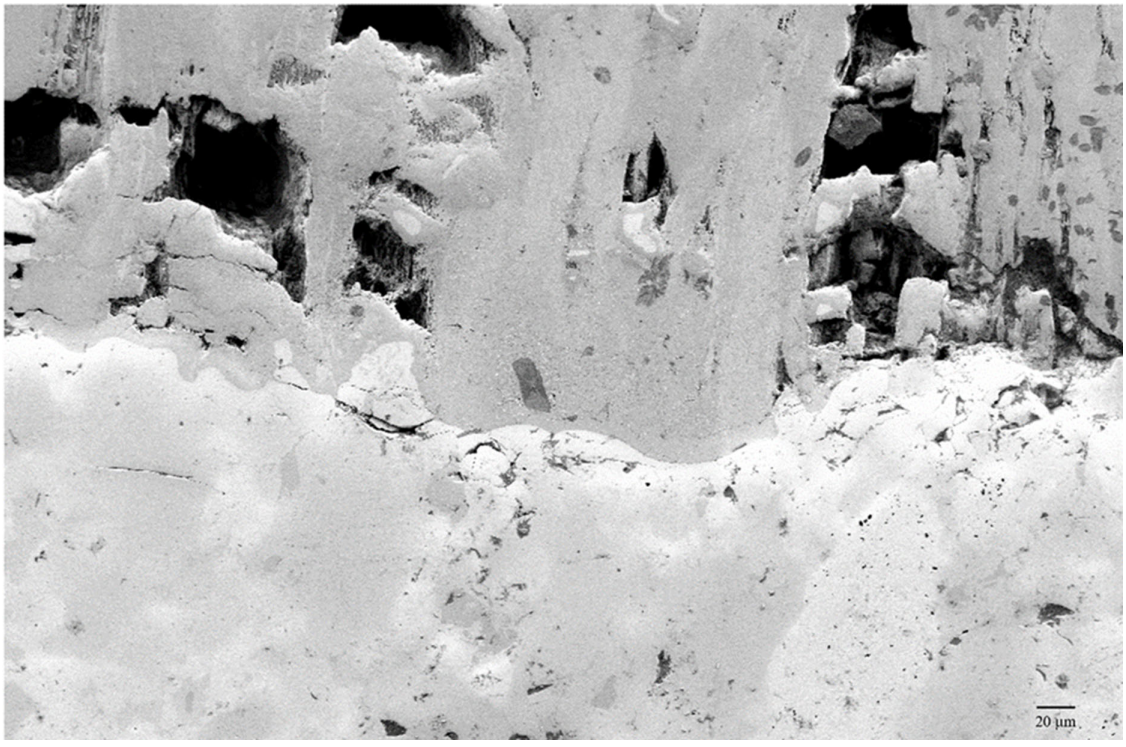

Figure 5. Substrate–oxide interface of the oxidized sample at 800 °C after 24 h in the SE mode with large, prominent pores just above the interface.

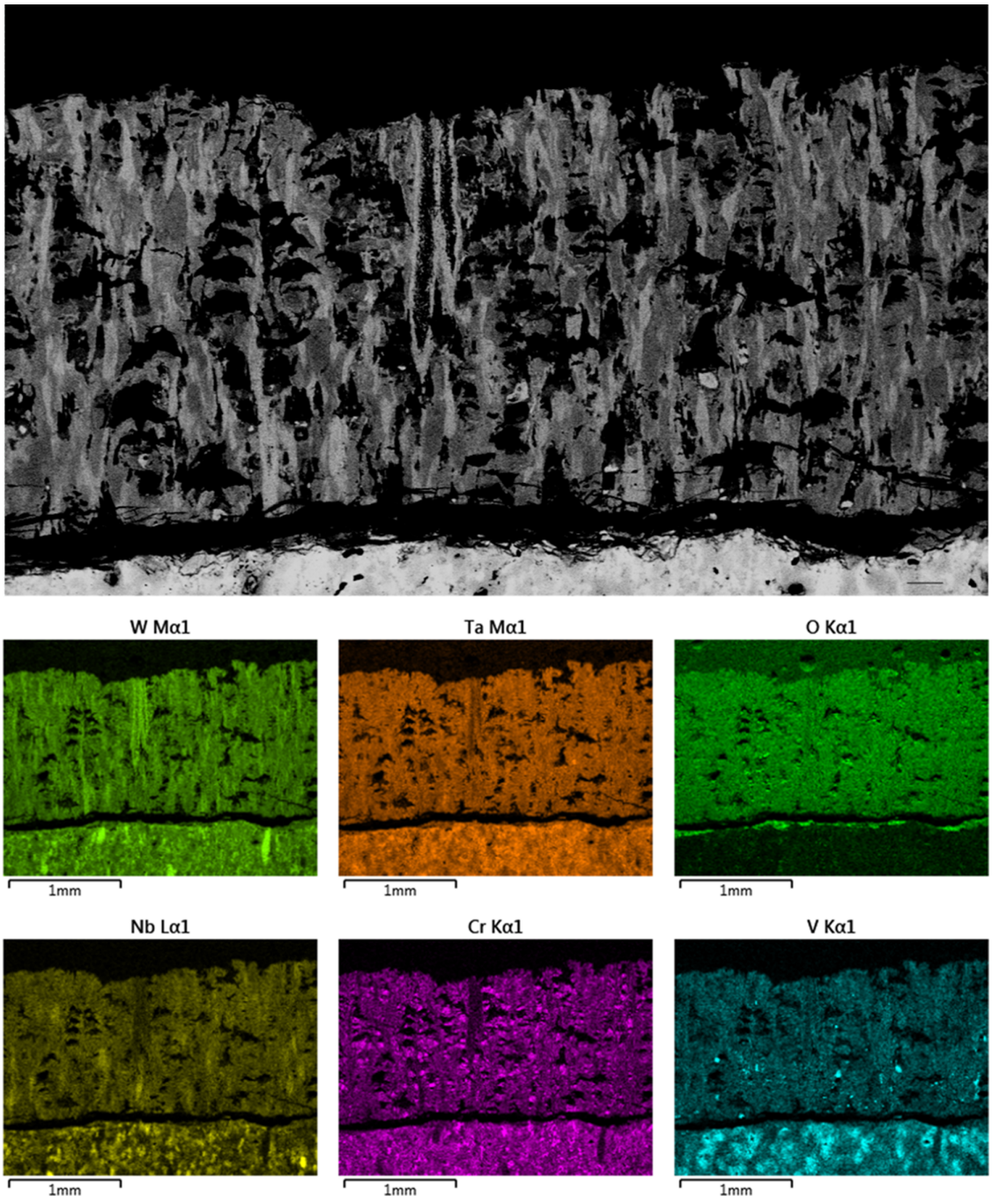

Figure 6. Substrate–oxide layer interface of the oxidized sample at 800 °C after 48 h in the BSE mode with EDS elemental mapping.

Figure 8 shows the top surface of the 700 °C sample oxidized for 48 h. Evidently, a very porous oxide, spread throughout the surface, can be seen. There are two prominent oxides present, one of a Cr-rich oxide with Ta and Nb present with small amounts of W and V. The Cr-rich oxide has a granular structure. Extending out of the Cr oxides are W oxide whiskers, which appear to be fine in nature. The W oxide whiskers are believed to be the other main oxide present, which grow outward and appear as the lighter structures in the image. This is the most prominent oxide present on the top surface of the oxide layer.

The 800 °C sample oxidized for 48 h can be seen in **Figure 9**. The structure is similar to that of the 700 °C sample; however, the W oxides are more prevalent and have become more defined. The difference in the oxide structure at the surface can be seen in **Figure 10**. The most prominent oxides present

Figure 7. Substrate–oxide interface of the oxidized sample at 800 °C after 48 h in the BSE mode, indicating the thickness of the oxide layer.

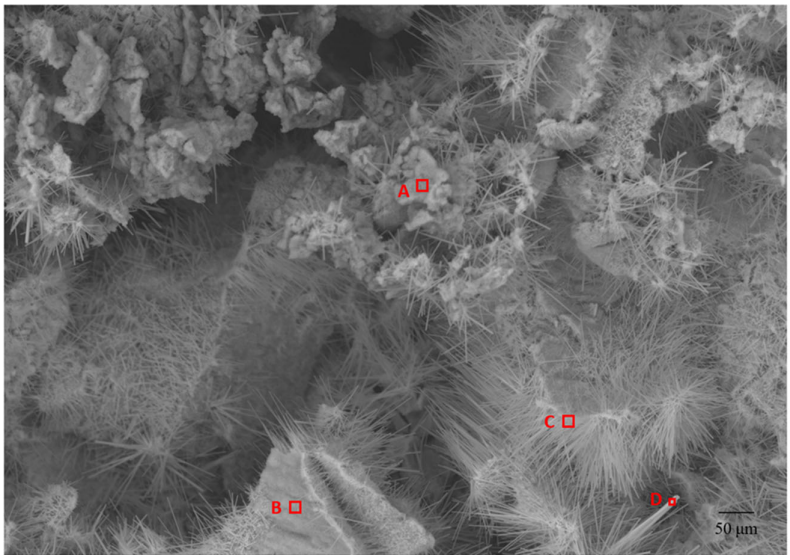

	A	B	C	D
O	49.78	54.05	62.25	53.47
V	4.43	9.01	3.53	4.24
Cr	20.69	11.99	3.83	3.11
Nb	8.06	6.91	5.53	7.55
Ta	12.06	9.69	10.98	12.60
W	4.98	8.35	13.88	19.03
Total	100.0	100.0	100.0	100.0

Figure 8. Surface of the oxide layer at 700 °C after 48 h in the BSE mode. The two main oxides are visible, the granular Cr oxide containing Ta and Nb with low amounts of V and W present. A whisker-like W oxide growing outward from the Cr oxide.

are once again a Cr oxide and a W oxide. The W oxide has grown longer and thicker than what was seen on the previous sample. This is indicative that the oxides grow with an increase in temperature. The granular Cr oxide is once again present but has become more defined and has a higher Cr content than at 700 °C. Both images utilized EDS to confirm the chemical compositions of the oxides.

2.3. Oxide Growth—High-Temperature XRD

In situ high-temperature XRD was performed on an unoxidized sample with 100 °C increments up to 800 °C to understand the oxide growth with increasing temperature. **Figure 11** shows the XRD data stacked vertically in terms of varying temperature. At 100 °C, there are little to no indications of oxide growth. The

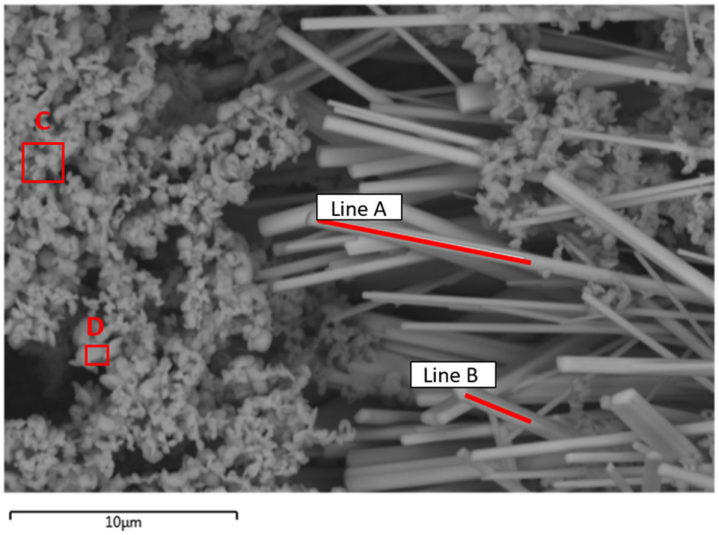

	Line A	Line B	C	D
O	70.8	73.8	58.0	54.3
V	2.2	2.5	3.7	5.1
Cr	1.2	0.0	20.0	16.5
Nb	8.0	7.3	6.7	7.4
Ta	5.6	5.8	8.1	8.0
W	12.2	10.6	3.5	8.7
Total	100.0	100.0	100.0	100.0

Figure 9. Surface of the oxide layer of the 800 °C after 48 h sample in the BSE mode. The granules of the Cr oxide have become more defined and contain a higher content than that seen at 700 °C. The W oxide has become thicker and is more prominent.

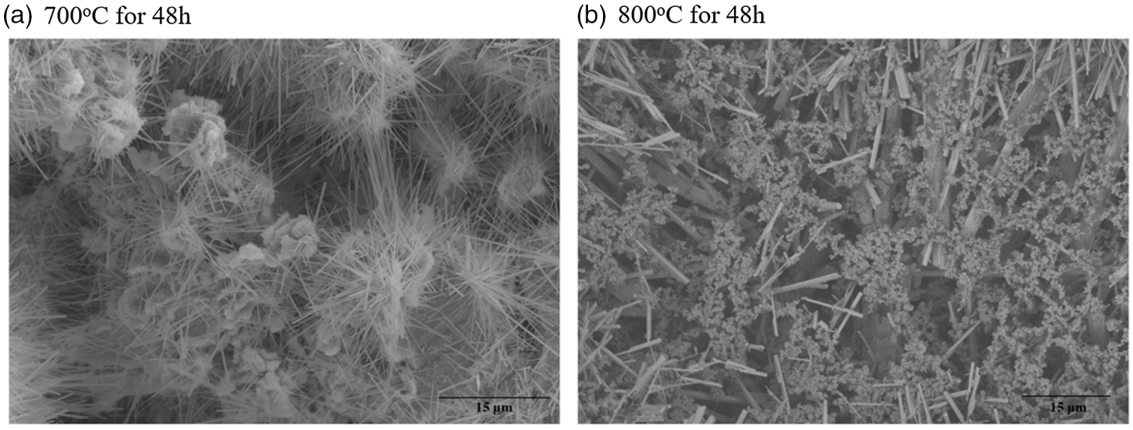

Figure 10. Surface of the oxide layer at a) 700 °C for 48 h and b) 700 °C for 48 h. The difference between the morphology is visible.

main peaks identified are of metal compounds, except for Cr, which did not appear as a peak for any compounds. This continues as the temperature increases up till 500 °C. There are small peaks of different V oxides, indicating that V is the first element to oxidize. The peaks of V oxides change from V_7O_3 and $V_{14}O_6$ to VO_2 at 600 °C, indicating that more oxygen is introduced into the system at higher temperatures. There is no indication of any proven type of protective oxides previously identified, including $CrTaO_4$ and Cr_2O_3.[32] At both 700 and 800 °C, peaks of NbO_2 and WO_3 are identified. Nb_2O_5 peaks also appear at 800 °C, though this was not found in the cross section of the sample. None of the identified oxides suggested by the experimental data is protective, indicating that oxygen can diffuse into the material faster and explain for the denser oxide layer at higher temperatures.

The SEM and EDS analysis performed in conjunction with the XRD analysis provided further insight how this material oxidizes, and the oxide layer forms. The XRD results showed up V oxide peaks forming at lower temperatures; however, this did not appear in the cross-sectional or oxide surface layers. This may potentially be due to the low melting point of some V oxides that create porous structures. Because the sample was only held at temperature for 20 min during the in situ XRD, this most likely did not allow enough time for the oxide to melt and allowed for the detection of the V oxides, but when held for longer periods, the oxide was able to melt and was only detected near the interface, leaving large pores throughout the structure. Tungsten appeared throughout the oxide layer and at the surface at both 700 and 800 °C, which explains for the detection of WO_3. This is believed to be the elongated, whisker-like oxide found at the surface and vertically throughout the cross-sectional layer. It is possible that if the samples could oxidize at these temperatures for longer times, the individual oxides may form solid solutions or mixed spinels. Additional XRD measurements must be conducted on the oxides scales to confirm this.

These results may shed some light on the effectiveness of the use of refractory metals in the HEA composition for surface and interface oxidation of the alloy. Although the oxidation rates of

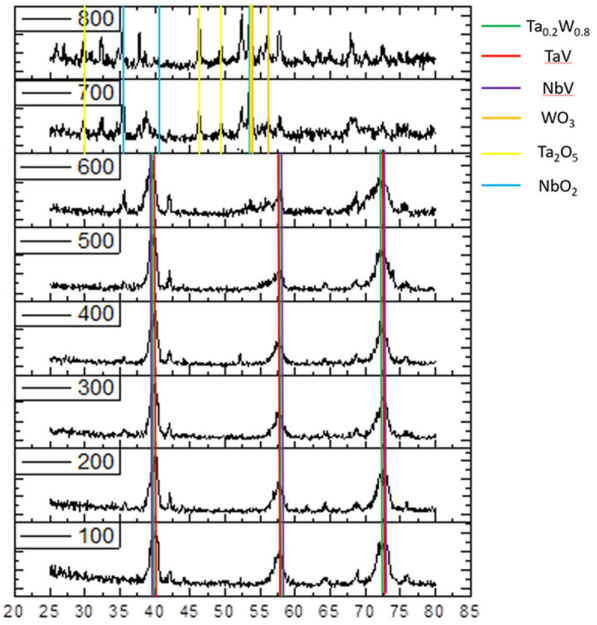

Figure 11. In situ XRD data of the HEAs.

pure refractory metals, W, Ta, and Nb, are higher at elevated temperatures than those employed in this work, the observed trends and differences at 700–800 °C in these HEAs can be still accountable to their respective oxide formation. Undoubtedly, as evident in SEM and EDS analyses, all the metals in the HEA oxidize and form their respective solid oxides. However, the outward growth of W oxide, which also is the most prominent oxide present on the top surface of the oxide layer as indicated by the SEM and EDS analyses, may be due to higher oxidation rate of W compared with Nb and Ta. Because of the significant presence of the W oxide throughout the oxide layer, it may be beneficial to replace this element with another element, such as Mo. Using Mo has seen in other HEAs and may be favorable for this particular alloy. The use of V in this alloy demonstrated to be detrimental to the oxidation resistance. It was the first element which appeared to oxidize and believed to influence the cracking and porosity seen at the interface. Evaluation of the mechanical properties of the alloy, including compression and hardness tests at both room and elevated temperatures, needed. Such studies may facilitate to find replacement and create an argument for V use in this alloy, although V is known for being beneficial to high-temperature strength and ductility. Therefore, additional studies on the mechanical properties, as well as the variation of the alloy composition, are considered for our future research direction.

3. Conclusions

The substrate–oxide layer interface of a CrNbTaWV high entropy alloy was oxidized at temperatures of 700 and 800 °C to examine the oxidation behavior of individual elements, the way in which oxides grow outward from the metal, and to characterize the morphology and compositions of the surface layer of the oxide layer. The key findings in this study are summarized as follows: 1) No specific indications of selective oxidation were found along the interface, though there is some Ta oxide that agglomerates near the interface. A significant amount of cracking and porosity was also found along the interface. Previous microstructures of this alloy composition were confirmed, including the phases previously indicated. 2) Many of the oxides cluster within the oxide layer. The only exception to this is W, which grows outward vertically within the layer. No protective oxides were identified, indicating that oxygen can diffuse into the material faster, which explains the dense structure of the oxide layer at a higher temperature. 3) A Cr-rich oxide containing Ta has a granular morphology that is more apparent at 700 °C. There were trace amounts of Nb found within the oxide. A W oxide was also found, as a long, whisker-like morphology. This was believed to be WO_3 based on the XRD results. 4) The increase in temperature causes an increase in oxide scale growth. The thickness of the oxide layer was thicker at 800 °C than at 700 °C; however, the oxide thickness varies (530–1132 μm) at 700 °C. 5) The in situ XRD results indicate that the first element to oxidize is V, which begins around 500 °C. The peaks of V oxides change from V_3O_7 and $V_{14}O_6$ to VO_2 at 600 °C, indicating that more oxygen is introduced into the system at higher temperatures. NbO_2 and WO_3 begin to appear at 700 °C, along with Nb_2O_5; however, this was not able to be confirmed with EDS in the cross section of the sample.

4. Experimental Section

Cr–Nb–Ta–V–W HEAs: Oxidation studies were performed on 5 mm × 5 mm × 5 mm cubes of equiatomic Cr–Nb–Ta–V–W high entropy alloy. The cubes of Cr–Nb–Ta–V–W HEAs were procured from Plasma Materials Inc. (Livermore, CA, USA) and were made by arc melting using metals of at least three nines purity. The as-received cubes were cut by electrical discharge machining (EDM). Two specimens were oxidized from the as-received state in a muffle box air furnace placed in an alumina crucible, at 700 and 800 °C, respectively, for 24 h. These samples were subjected to cross-sectional SEM and EDS analysis. The third specimen (as-received) was subjected to high-temperature in situ XRD analysis to determine oxide growth patterns. Two more specimens were also oxidized from the as-received state for 48 h, one at 700 °C and one at 800 °C, so that the surface oxide layer could be examined. Samples were oxidized in an air furnace (Muffle Box Furnace, Sentrotech, Strongville, OH, USA) with computer-controlled heating and cooling cycles for isothermal heating. A heating rate of 10 °C min^{-1} was utilized up to the selected oxidation temperature. The samples were then cooled to room temperature inside the furnace.

Metallographic Sample Preparation: Cross-sectional analysis of the oxidized samples was facilitated using precision cutoff machines set to a cutting rate of 0.005 mm s^{-1}, utilizing an abrasive cutting disk. Before cutting, the samples were stabilized using a two-component epoxy adhesive. The purpose of the adhesive is to fill any open gaps and provide more stability when cutting, grinding, and polishing the sample. Previous attempts to cut the sample without reinforcement led to separation of the oxide from the remaining metal core. The samples were polished using a series of diamond discs ranging from 220 grit to 8 μm, followed with an alcoholic diamond suspension, then a Al_2O_3 oxide suspension (Masterprep), before completing a final cleaning with detergent and water for 20 min. All polishing was done with an applied pressure of 10 N.

SEM and EDS: Microstructural analysis of the preoxidized samples was done in SEM (DSM Ultra 55, Carl Zeiss NTS, Wetzlar, Germany) equipped with EDS (Inca, Oxford Instruments, Abingdon, UK) system. The EDS system did not use standards. EDS elemental mapping, in conjunction with area and spot analysis of the captured images, was done to determine the

chemical composition of the final oxides, transition layer, and remaining metallic structure of the samples. To observe the oxidized surface layer, SEM (Hitachi High-Tech America, Inc., USA) was performed using the backscattered electron and secondary electron mode. The EDS system did not use standards. The compositions of the oxides were determined by EDS with the use of X-ray color mapping to allow for the determination of elements.

High-Temperature XRD: To understand the oxide evolution of the high entropy alloy at elevated temperatures, the as-received alloy sample was measured in a static lab air high-temperature XRD system (D8 Advance with Cu Kα radiation and Lynxeye detector Bruker AXS, Karlsruhe, Germany). To maintaining consistency with previously conducted experiments, and to allow for a direct comparison with the two oxidized samples, the alloy was heated to a maximum temperature of 800 °C with a heating rate of 10° min^{-1}. Measurements were taken at 100 °C intervals starting at 100 °C and continuing through 800 °C. At each interval, the temperature was kept constant for 20 min to allow for stabilization before actual measurements commenced for 30 min. With final measurements completed, the sample was air-cooled to room temperature.

Acknowledgements

R.R., and N.M. contributed equally to this work. This work is a contribution from the Center for Advanced Materials Research (CMR). The authors at the University of Texas at El Paso acknowledge, with pleasure, support from the National Science Foundation with NSF-PREM grant #DMR-1827745.

Conflict of Interest

The authors declare no conflict of interest.

Data Availability Statement

Data related to this work are included in the manuscript.

Keywords

microstructure, Nb–Cr–V–W–Ta, oxidation, refractory high entropy alloys

Received: February 6, 2021
Revised: April 11, 2021
Published online: May 18, 2021

[1] J. W. Yeh, S. K. Chen, S. J. Lin, J. Y. Gan, T. S. Chin, T. T. Shun, C. H. Tsau, S. Y. Chang, *Adv. Eng. Mater.* **2004**, *6*, 299.
[2] J. Yeh, S. Chen, J. Gan, S. Lin, T. Chin, *Metall. Mater. Trans. A* **2004**, *35*, 2533.
[3] C. J. Tong, Y. L. Chen, S. K. Chen, J. W. Yeh, T. T. Shun, C. H. Tsau, S. J. Lin, S. Y. Chang, *Metall. Mater. Trans. A Phys. Metall. Mater. Sci.* **2005**, *36*, 881.
[4] J. W. Yeh, S. Y. Chang, Y. Der Hong, S. K. Chen, S. J. Lin, *Mater. Chem. Phys.* **2007**, *103*, 41.
[5] D. B. Miracle, O. N. Senkov, *Acta Mater.* **2017**, *122*, 448.
[6] S. Gorsse, D. B. Miracle, O. N. Senkov, *Acta Mater.* **2017**, *135*, 177.
[7] J. Chen, X. Zhou, W. Wang, B. Liu, Y. Lv, W. Yang, D. Xu, Y. Liu, *J. Alloys Compd.* **2018**, *760*, 15.
[8] T. I. Williams, *Endeavour* **1988**, *12*, 193.
[9] M. H. Tsai, J. W. Yeh, *Mater. Res. Lett.* **2014**, *2*, 107.
[10] C. C. Juan, M. H. Tsai, C. W. Tsai, C. M. Lin, W. R. Wang, C. C. Yang, S. K. Chen, S. J. Lin, J. W. Yeh, *Intermetallics* **2015**, *62*, 76.
[11] D. H. Xiao, P. F. Zhou, W. Q. Wu, H. Y. Diao, M. C. Gao, M. Song, P. K. Liaw, *Mater. Des.* **2017**, *116*, 438.
[12] H. W. Yao, J. W. Qiao, M. C. Gao, J. A. Hawk, S. G. Ma, H. F. Zhou, Y. Zhang, *Mater. Sci. Eng. A* **2016**, *674*, 203.
[13] Y. J. Zhou, Y. Zhang, Y. L. Wang, G. L. Chen, *Appl. Phys. Lett.* **2007**, *90*, 181904.
[14] O. N. Senkov, G. B. Wilks, D. B. Miracle, C. P. Chuang, P. K. Liaw, *Intermetallics* **2010**, *18*, 1758.
[15] O. N. Senkov, G. B. Wilks, J. M. Scott, D. B. Miracle, *Intermetallics* **2011**, *19*, 698.
[16] O. N. Senkov, C. F. Woodward, *Mater. Sci. Eng. A* **2011**, *529*, 311.
[17] X. Xian, Z. Zhong, B. Zhang, K. Song, C. Chen, S. Wang, J. Cheng, Y. Wu, *Mater. Des.* **2017**, *121*, 229.
[18] Z. D. Han, H. W. Luan, X. Liu, N. Chen, X. Y. Li, Y. Shao, K. F. Yao, *Mater. Sci. Eng. A* 20182017, *712*, 380.
[19] O. N. Senkov, C. Woodward, D. B. Miracle, *JOM* **2014**, *66*, 2030.
[20] O. N. Senkov, S. V. Senkova, C. Woodward, *Acta Mater.* **2014**, *68*, 214.
[21] S. K. Varma, F. Sanchez, C. V. Ramana, *J. Mater. Sci. Technol.* **2020**, *53*, 66.
[22] B. Gorr, M. Azim, H. J. Christ, T. Mueller, D. Schliephake, M. Heilmaier, *J. Alloys Compd.* **2015**, *624*, 270.
[23] B. Gorr, F. Müller, M. Azim, H. J. Christ, T. Müller, H. Chen, A. Kauffmann, M. Heilmaier, *Oxid. Met.* **2017**, *88*, 339.
[24] B. Gorr, F. Mueller, H. J. Christ, T. Mueller, H. Chen, A. Kauffmann, M. Heilmaier, *J. Alloys Compd.* **2016**, *688*, 468.
[25] T. M. Butler, J. P. Alfano, R. L. Martens, M. L. Weaver, *JOM* **2015**, *67*, 246.
[26] S. K. Varma, F. Sanchez, S. Moncayo, C. V. Ramana, *J. Mater. Sci. Technol.* **2020**, *38*, 189.
[27] C. M. Liu, H. M. Wang, S. Q. Zhang, H. B. Tang, A. L. Zhang, *J. Alloys Compd.* **2014**, *583*, 162.
[28] J. G. Speight, *Lange's Handbook of Chemistry*, 16th edn., CD&W, Inc., Laramie, WY **2005**.
[29] P. Hidnert, *Bur. Stand. J. Res.* **1929**, *2*, 887.
[30] P. Hidnert, W. T. Sweeney, *Sci. Pap. Bur. Stand.* **1925**, *20*, 483.
[31] Y. Xiao, W. Kuang, Y. Xu, L. Wu, W. Gong, J. Qian, Q. Zhang, Y. He, *J. Mater. Res.* **2019**, *34*, 301.
[32] K. C. Lo, Y. J. Chang, H. Murakami, J. W. Yeh, A. C. Yeh, *Sci. Rep.* **2019**, *9*, 3.